

O. MOUTANABBIR<sup>1,\*</sup>,  
B. TERREAULT<sup>1</sup>  
M. CHICOINE<sup>2</sup>  
F. SCHIETTEKATTE<sup>2</sup>

## The fluence effect in hydrogen-ion cleaving of silicon at the sub-100-nm scale

<sup>1</sup> INRS-EMT, Université du Québec, 1650 Boul. Lionel-Boulet, Varennes, Québec J3X 1S2, Canada

<sup>2</sup> Département de Physique, Université de Montréal, C.P. 6128, Succ. Centre-Ville, Montréal, Québec H3C 3J7, Canada

Received: 26 July 2004/Accepted: 18 October 2004

Published online: 25 November 2004 • © Springer-Verlag 2004

**ABSTRACT** The implementation at the sub-100-nm scale of ion cleaving requires ion beams of  $\sim 5$  keV/amu or less. The blistering efficiency in 5-keV H-ion-implanted and annealed Si has been found to peak and vanish in a narrow range of ion fluence of  $(1.5\text{--}3.5) \times 10^{16}$  H/cm<sup>2</sup>. In order to understand this effect, the defect profiles in 5-keV H-irradiated Si were studied by Rutherford backscattering/channelling, while the Si–H bonding configurations during annealing were investigated by Raman scattering spectroscopy. Three types of defects play major roles: the ‘broad-band’ monohydride multivacancy complexes, the fully or partially passivated monovacancy  $VH_n$ , and H-terminated internal surfaces Si(100):H. Blister absence at high fluence is characterised by the persistence up to 550 °C of the Si(100):H structures, which are blister embryos that failed to coalesce and grow. Radiation-induced stresses and fracture toughening may play roles in inhibiting cleavage at high fluence; however, widening towards the surface of the zone of high H and defect concentration is the likely major factor.

PACS 61.82.Fk; 82.80.Gk; 61.85.+p

### 1 Introduction

Ion blistering, flaking, exfoliation, or cleaving are generic phenomena frequently observed when insoluble light ions (H, He) are implanted in various solids: metals, semiconductors, and insulators [1]. It may take place at low temperature as a result of high-fluence implantation (generally several times  $10^{17}$  ions/cm<sup>2</sup>), or as a result of lower-fluence implantation ( $\leq 10^{17}$  ions/cm<sup>2</sup>) followed by high-temperature annealing. The phenomenological similarity in ion cleaving of different materials by different ions hides in reality a diversity of microscopic mechanisms responsible for the final outcome. Only the study of these mechanisms can help to understand and control this sometimes puzzling process. For instance, in H-ion cleaving of silicon, discovered in the 1970s [2, 3], the role of Si–H chemistry was shown to be decisive [4].

Ion cleaving, considered a nuisance until the mid-1990s as a cause of degradation of fusion-reactor walls [1] or semiconductor surfaces [5], suddenly attracted much inter-

est following its ingenious use by Bruel [6] to bond thin Si layers on high-quality SiO<sub>2</sub> – the so-called Smart-Cut<sup>®</sup> process of silicon-on-insulator fabrication. As commonly used [4, 6–11], Si cleaving is accomplished by implantation of H ions with energies of tens of keV up to over 100 keV, resulting in cleaved layers of several hundred nanometres up to microns (of the order of the mean ion projected range). As device dimensions shrink, there is an obvious motivation to reduce the thickness of the cleaved layer. In the industrial process, the final desired thickness is adjusted by chemical–mechanical polishing. However, one may wish to reduce or eliminate polishing for some future applications, and this can be done by reducing the ion energy to a few keV. In addition, it is fundamentally interesting and challenging to explore the limits of the process, considering that the nature of ion–solid interactions evolves in this energy range [12]: the elastic losses become dominant over the electronic losses, though this effect is counterbalanced by a quasi-unavoidable channelling.

Another practical point is to find the optimal ion dose leading to neat cleavage while minimising the time and cost involved as well as the radiation damage introduced into the wafer. In this work, we investigated the ion-fluence dependence and the underlying mechanisms of cleaving of silicon by H ions of 5 keV/amu, corresponding to a mean projected range,  $R_p$ , of  $\sim 80$  nm [13]. For this purpose, we used Rutherford backscattering in the channelling mode (RBS/C) to determine the implantation damage profiles and Raman scattering spectroscopy (RSS) together with thermal desorption spectrometry (TDS) to scrutinise the chemical evolution of the hydrogen under annealing up to the cleaving temperature.

### 2 Experiment

Cz-grown *n*-type (100) Si wafers (1–10 Ω cm resistivity) were cut into 1 cm<sup>2</sup> pieces, ultrasonically cleaned with solvents, and subsequently implanted at room temperature (RT) with 10-keV H<sub>2</sub><sup>+</sup> molecular ions at a number of total fluences ranging from  $1 \times 10^{16}$  to  $2 \times 10^{17}$  H atoms per cm<sup>2</sup>. The samples did not significantly heat up during implantation since the beam power is only  $\sim 10$  mW/cm<sup>2</sup>. The base pressure of the implanter is  $< 10^{-7}$  mbar.

On some samples, we used channelling in combination with Rutherford backscattering spectrometry (RBS/C) in order to obtain the defect profiles [14]. The RBS/C measurements were done on the 1.7-MV Tandatron accelerator at the

✉ Fax: +1-450-929-8102, E-mail: moutanabbir@inrs-emt.quebec.ca  
\*Present address: Department of Applied Physics and Physico-Informatics, Keio University, 3-14-1, Hiyoshi, Kohoku-ku, Yokohama 223-8522, Japan

Université de Montréal using a 2-MeV He<sup>+</sup> beam. The channelling direction was found with a precision better than 0.1° by interpolating between planar channelling directions. The incident beam was defined by a 2-mm-diameter aperture. The typical beam current was 5 nA. Each time, the current on the target was confirmed by a current measurement in a Faraday cup. The outgoing particles were detected by a movable passivated implanted planar silicon (PIPS) detector with ~15-keV energy resolution. The sample-detector distance and detection solid angle were 122 mm and 6.7 mSr, respectively.

To investigate the temperature evolution of Si–H interactions, Raman scattering spectroscopy (RSS) analyses were accomplished on identical samples with a Renishaw 3000 Raman system having a resolution of 2 cm<sup>-1</sup>. The excitation was supplied by an Ar-ion laser (514.5 nm, 25 mW) at normal incidence. The laser light was focused on the sample surface through a ×50 objective lens; the diameter of the focused laser spot was about 3 μm. The scattered light was collected at RT by a CCD detector (collection time: 500 s, averaging factor: 4), and the background luminescence was subtracted from the data. The annealing protocol was the following: the samples were subjected to a linear ramp of 20 °C/min up to a target temperature, e.g. 200 °C, let to cool to RT for measurement, and then ramped up again to a higher temperature, and so on until 550 °C. The RSS spectra are all normalised with respect to the data at RT. The identification of particular features in the Raman spectra with specific vibration modes associated with specific structures is a complicated task, but the Si–H stretch modes in the region 1800–2300 cm<sup>-1</sup> have been widely investigated [4, 15–21]. We have used these last references as guidelines; the details are given in our earlier paper [22].

Afterwards, the surface topography of the samples was observed by atomic force microscopy (AFM) in contact mode with a Nanoscope IIIa (Digital Instruments) on at least five different spots. The morphology was quantified and statistically analysed using the WSxM program [23]. Finally, iden-

tical samples were thermally desorbed in vacuum using the same ramp of 20 °C/min while the H<sub>2</sub> partial pressure was monitored by a quadrupole mass spectrometer (UTI Detec-Torr). Thermal desorption spectrometry (TDS) thus allows one to correlate bursts of hydrogen emission at particular temperatures with the evolution of the Si-bound H (Raman).

### 3 Results

#### 3.1 Surface morphology

We show in Fig. 1 a representative sub-set of AFM images of implanted and annealed samples, with fluences ranging from  $1 \times 10^{16}$  to  $6 \times 10^{16}$  H/cm<sup>2</sup>. For a fluence of  $1 \times 10^{16}$  H/cm<sup>2</sup> (Fig. 1a), the surface is roughened on the nanometre scale but unblistered yet. For a fluence of  $1.5 \times 10^{16}$  H/cm<sup>2</sup> (Fig. 1b), small blisters with a diameter generally less than 0.5 μm have appeared. The surface for  $2 \times 10^{16}$  H/cm<sup>2</sup> (Fig. 1c) is fully blistered, with blister diameters between 0.5 and 1 μm and heights of 15–20 nm. At  $3.5 \times 10^{16}$  H/cm<sup>2</sup> (Fig. 1d), the morphology has visibly changed. Many blisters have exfoliated, a sign of the higher gas pressure due to the higher H dose; however the blister density appears lower than at  $2 \times 10^{16}$  H/cm<sup>2</sup>. For  $4.5 \times 10^{16}$  H/cm<sup>2</sup> (Fig. 1e), only scattered blisters are seen and, for  $6 \times 10^{16}$  H/cm<sup>2</sup> (Fig. 1f), the surface is featureless. Essentially identical results were obtained on samples that were rapid-thermal annealed in vacuum with an infrared lamp (up to ~600 °C in ~30 s) [24]. Figure 2 shows the results of a quantitative analysis of the blistered (or exfoliated) area as a function of fluence. This intriguing inhibition of cleavage at higher fluence had been hinted at in the literature [25] but never systematically studied. Finally, for much higher fluences (~ $2 \times 10^{17}$  H/cm<sup>2</sup>), blistering does reappear, but this time at RT without annealing, see Fig. 3. Of course this last case is less interesting for device fabrication since it does not allow bonding to another wafer prior to cleaving.

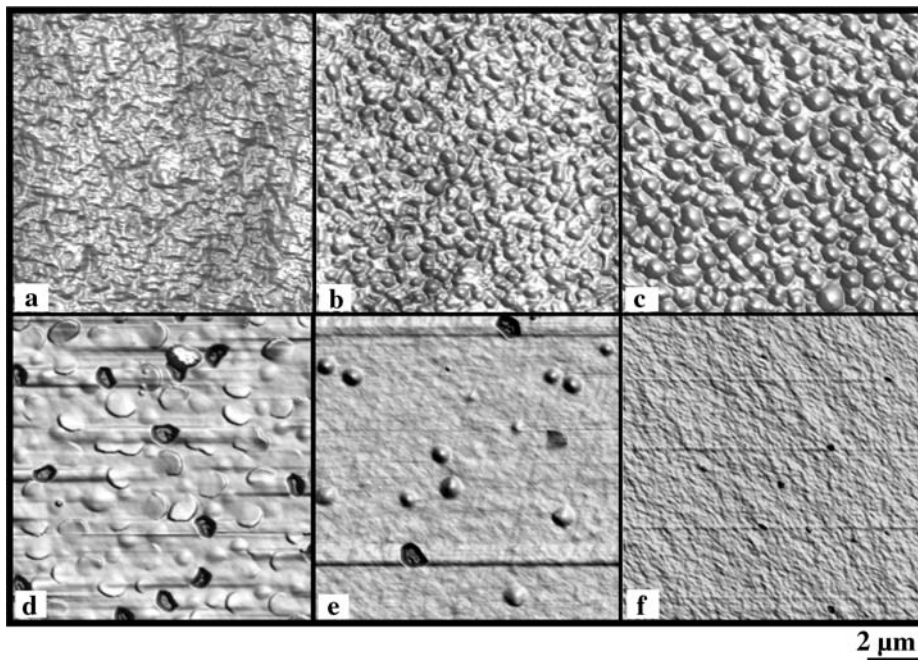


**FIGURE 1** Atomic force microscopy images of low-doped Si(100) implanted at room temperature with 5-keV/amu H ions to fluences of (a)  $1 \times 10^{16}$  H/cm<sup>2</sup>, (b)  $1.5 \times 10^{16}$  H/cm<sup>2</sup>, (c)  $2 \times 10^{16}$  H/cm<sup>2</sup>, (d)  $3.5 \times 10^{16}$  H/cm<sup>2</sup>, (e)  $4.5 \times 10^{16}$  H/cm<sup>2</sup>, (f)  $6 \times 10^{16}$  H/cm<sup>2</sup>

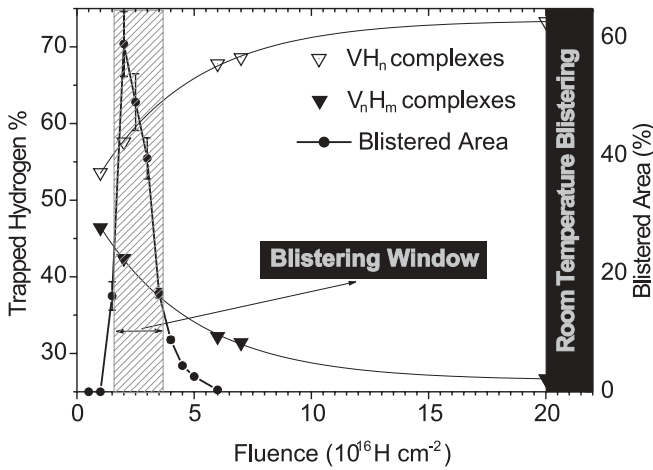


**FIGURE 2** Correlation of surface morphology with Raman spectral features. Plotted as a function of H-ion fluence are shown the actual blistered area after annealing and the integrated room-temperature Raman signals due to ‘ $V_nH_m$ ’ complexes ( $LF < 2050 \text{ cm}^{-1}$ ) and ‘ $VH_n$ ’ complexes ( $HF > 2050 \text{ cm}^{-1}$ ). The blistering ‘window’ is indicated by shading

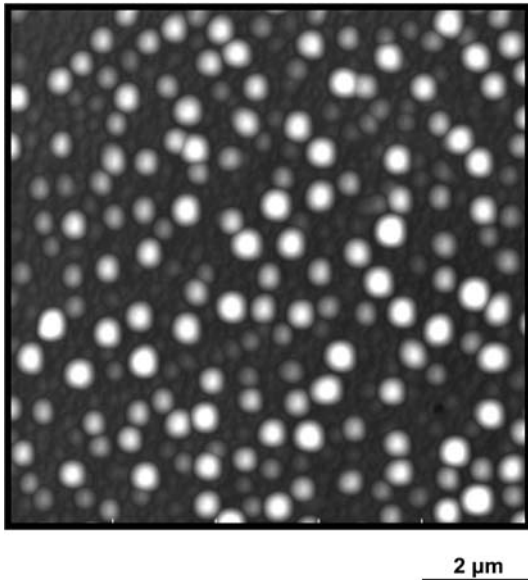


**FIGURE 3** Low-resolution AFM image of room-temperature blistering for  $2 \times 10^{17} \text{ H/cm}^2$

### 3.2 Atomic displacement profiles

Since implanted H is known by numerous previous studies to be trapped by defects in Si, we measured the depth profiles of displaced atoms by RBS/channelling for three different H fluences, corresponding to a sub-threshold fluence ( $1 \times 10^{16} \text{ H/cm}^2$ ), to that of maximum blistering ( $2 \times 10^{16} \text{ H/cm}^2$ ), and to high-fluence blister absence ( $6 \times 10^{16} \text{ H/cm}^2$ ). In Fig. 4 are shown the backscattering yields, including for comparison that of a virgin sample (lowest curve) and that obtained in a random direction (highest curve). In the implanted zone (channels  $\sim 515$  to  $\sim 535$ ), the dechannelling yield increases as a function of fluence as expected; for  $6 \times 10^{16} \text{ H/cm}^2$ , the degree of disorder is fairly high at the peak of the profile, but it remains far below the random level. These levels of dechannelling are comparable to those found in previous work at similar H concentra-

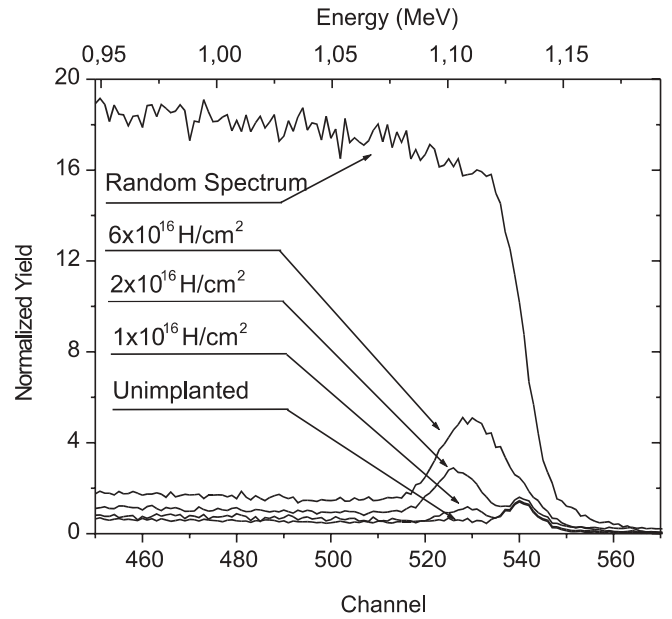


**FIGURE 4** RBS/C: normalised yields as a function of backscattered energy for, in order of increasing yield, a virgin sample, fluences of  $1 \times 10^{16}$ ,  $2 \times 10^{16}$ , and  $6 \times 10^{16} \text{ H/cm}^2$ , and a random direction

tions [9, 10, 26]. The Si interstitial profiles deconvoluted from Fig. 4 as a function of depth are shown in Fig. 5. In this plot, we also show the calculated profile of primary displaced atoms [13]. One can see that the actual experimental profiles are narrower than the computed one, which indicates that recombination or annihilation of defects preferentially takes place away from the peak, near the surface, and in depth. Both the vacancy and the self-interstitial are mobile in Si at RT but defect survival is more probable near the peak, presumably through clustering. In the substrate beyond the implanted zone (channels  $< 500$  in Fig. 4), the dechannelling yield is also increased by the implantation. This is attributed by Bedell and Lanford [10] to a distortion of the crystal, e.g. a slight lack of registry of the top implanted zone with respect to the substrate. It is interesting to note that this distortion is much smaller in our case; the dechannelling yield does not exceed 7% of the

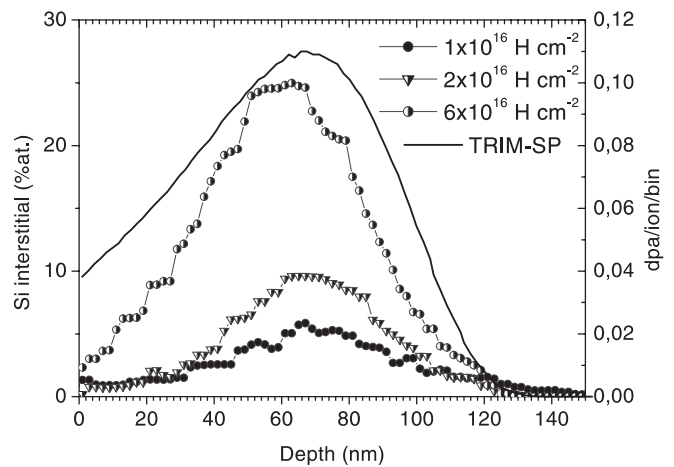


**FIGURE 5** Depth profiles of self-interstitials deconvoluted from Fig. 4 for the three implanted samples. A profile of primary defect production calculated by the code TRIM-SP [13] is also shown (arbitrarily normalised)

random level. In fact, in the previous data [9, 10, 26], there is a correlation between the implantation energy (40–175 keV) and the distortion (20%–50%) at a typical blistering fluence. It is thus natural to attribute this effect to the thickness of the distorted zone.

#### 4 RT Raman spectra

Post-implantation Raman spectra are shown in Fig. 6 for a number of different H fluences. One can readily observe that the spectra shift continuously towards higher

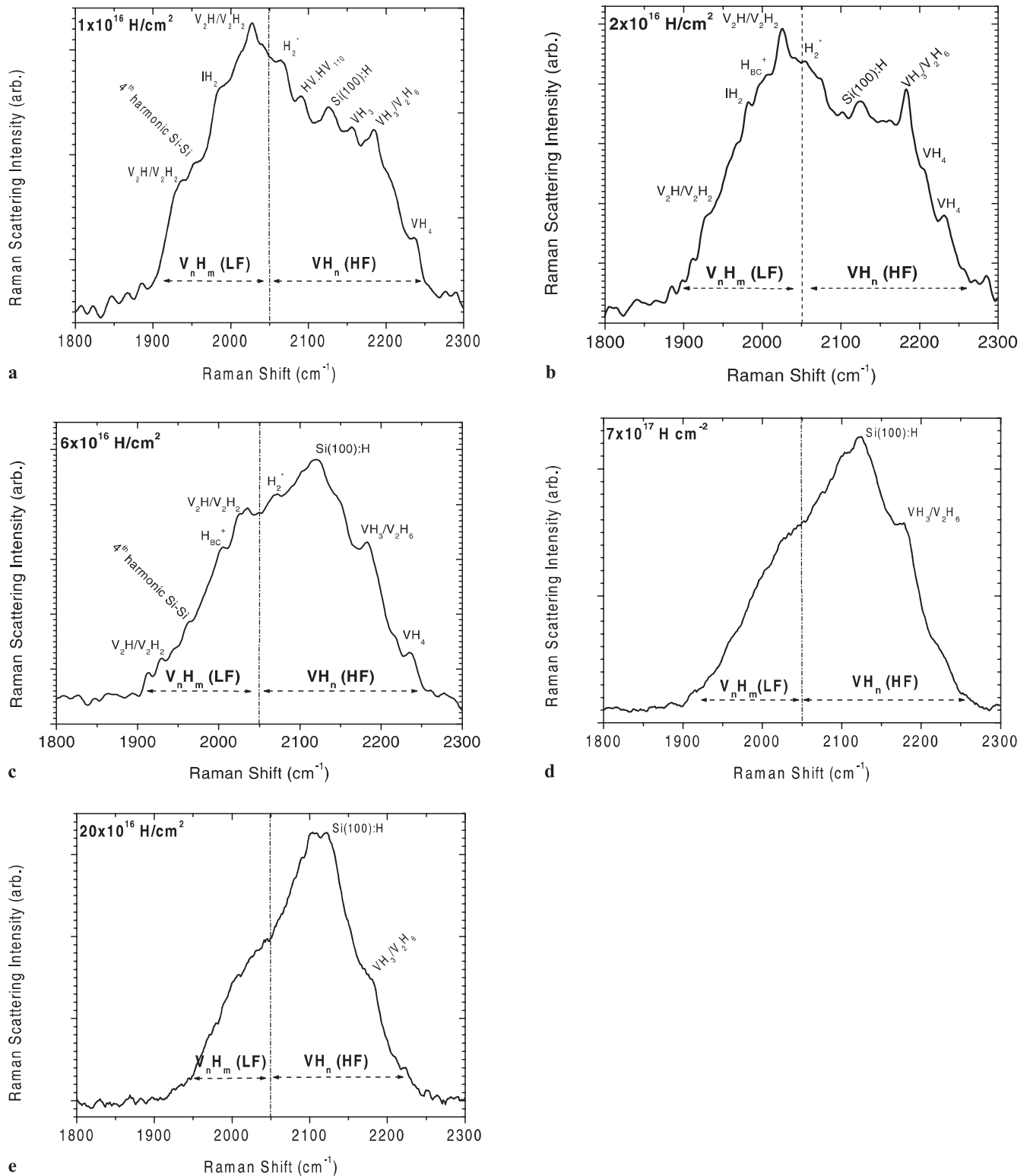


**FIGURE 6** Room-temperature stretch-mode region of Raman spectra following implantation of (a)  $1 \times 10^{16}$ , (b)  $2 \times 10^{16}$ , (c)  $6 \times 10^{16}$ , (d)  $7 \times 10^{16}$ , (e)  $2 \times 10^{17}$  H/cm<sup>2</sup>

frequencies as the fluence is increased. The lower-frequency broad band (LFBB), below  $2050\text{ cm}^{-1}$  approximately, is associated with hydrided multivacancies, denoted  $V_nH_m$ ,  $m \leq n$ , in highly disordered regions [4, 16]; a few well-identified peaks emerge above this broad band. The higher-frequency modes (HF  $> 2050\text{ cm}^{-1}$ ) are mostly due to multihydride single vacancies  $VH_n$ ,  $n = 2-4$ , or to H-terminated internal surfaces  $\text{Si}(100):\text{H}$ , shifted and broadened compared to the same modes on clean and atomically flat surfaces [16]. At the sub-threshold fluence ( $1 \times 10^{16}/\text{cm}^2$ ), the LF region dominates with relatively strong discrete modes. For  $2 \times 10^{16}\text{ H/cm}^2$ , the LF discrete modes tend to regress compared to the BB, due to the increasing disorder; in contrast, the HF modes take on more importance and in particular the mode due to either  $VH_3$  [4] or to  $V_2H_6$  [21]. Let us recall that this is the fluence where the maximum in blister coverage occurs after annealing (Fig. 2). It would thus seem that the HF complexes are the necessary ingredients for blistering. However, at higher fluence ( $6 \times 10^{16}/\text{cm}^2$ ), where no cleaving is observed upon annealing, the HF modes also clearly dominate and particularly the  $\text{Si}(100):\text{H}$  mode due to hydrided internal (100) surfaces. At even higher fluences, only that last peak clearly emerges and dominates; it appears that other modes are washed out by the high degree of radiation-induced disordering. For  $2 \times 10^{17}\text{ H/cm}^2$ , the strong accumulation of hydrogen on internal surfaces finally causes room-temperature blistering at that dose.

In Fig. 2, the integrated intensities of the LF and HF modes are plotted as a function of fluence. The fluence ‘window’ in which high-temperature cleaving takes place is also indicated, as well as the actual percentage of blistered area. This figure summarises the relationships between H-ion fluence, type of H trapping by defects, and surface morphology, e.g. no high-temperature cleaving when the HF modes exceed  $\sim 60\%$ .

#### 4.1 Temperature evolution

Let us now compare the evolutions as a function of temperature for the two most typical fluences,  $2 \times 10^{16}/\text{cm}^2$  and  $6 \times 10^{16}/\text{cm}^2$ , for a clue as to why only the lower one leads to cleavage. Figure 7 first shows the evolution of the integrated intensities of LF and HF modes. One can observe that the behaviour of the LF complexes (triangles) shows relatively little sensitivity to the H dose: in both cases they disappear progressively starting at  $200\text{ }^\circ\text{C}$ , and they do not seem to play a role in blistering. In reality, however, a strong presence at RT of the LFBB (as opposed to LF discrete modes) is a necessary condition for blistering [4, 22], although it is not a sufficient condition, as demonstrated by the data for  $6 \times 10^{16}\text{ H/cm}^2$ . The HF complexes (squares) evolve quite differently. For  $2 \times 10^{16}\text{ H/cm}^2$ , after an initial loss between  $200$  and  $300\text{ }^\circ\text{C}$ , the HF modes remain stable up to  $435\text{ }^\circ\text{C}$ , the approximate temperature of blistering. For  $6 \times 10^{16}\text{ H/cm}^2$ , HF modes are first lost between  $200$  and  $400\text{ }^\circ\text{C}$ , after which they are surprisingly stable up to quite high temperature – but never causing cleaving.

These broad features of H evolution can now be compared to the TDS results. Figure 8 shows both the total amount of Si-bound H (from Fig. 7) and the desorption rate as a function of annealing temperature. For  $2 \times 10^{16}\text{ H/cm}^2$  (Fig. 8a),

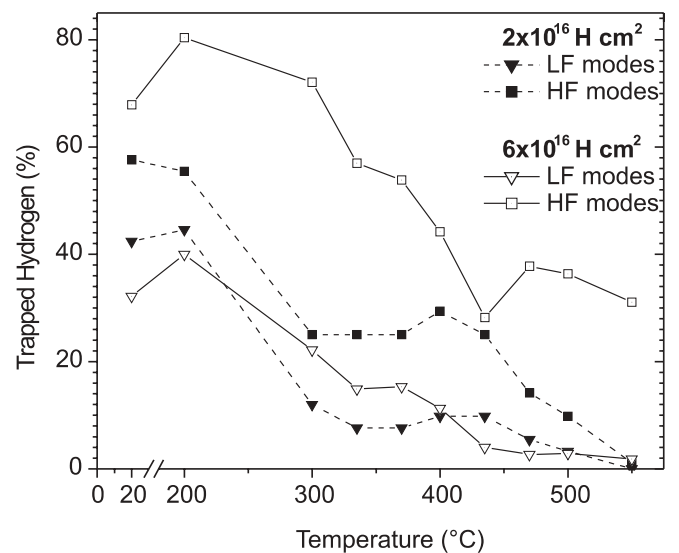


FIGURE 7 Evolution as a function of annealing temperature of LF and HF integrated intensities for fluences of  $2 \times 10^{16}$  and  $6 \times 10^{16}\text{ H/cm}^2$

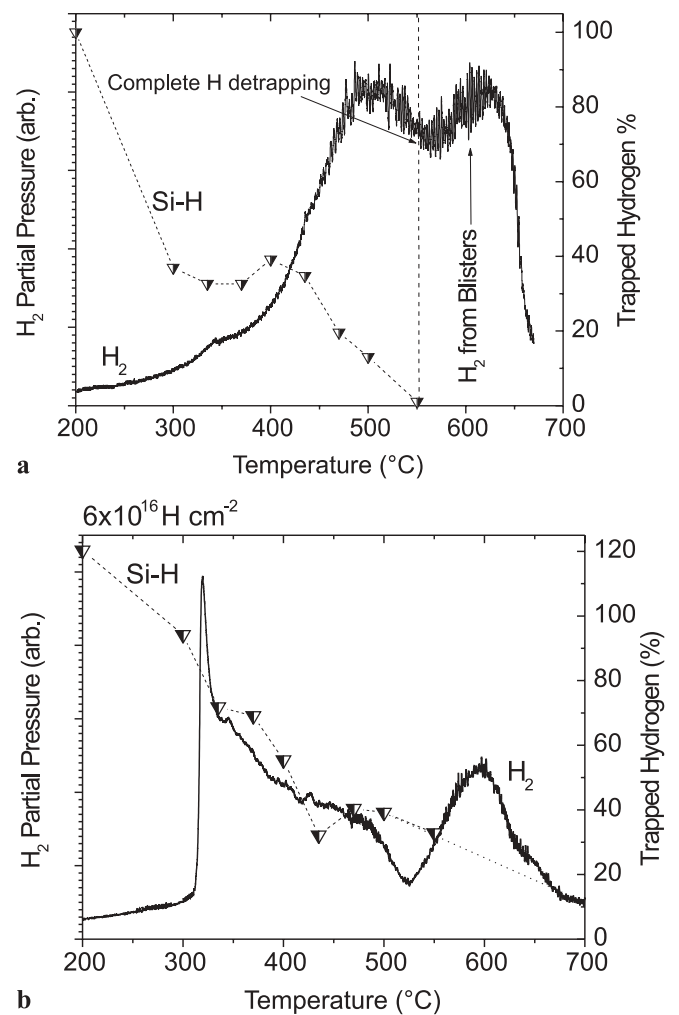


FIGURE 8 Correlation of the  $\text{H}_2$  thermal desorption yields (solid line) with the integrated Raman intensities (triangles) for fluences of (a)  $2 \times 10^{16}$  and (b)  $6 \times 10^{16}\text{ H/cm}^2$

it is seen that, below  $\sim 400^\circ\text{C}$ , the release of  $\text{H}_2$  is modest. Since much bound H disappears from the Raman integrated signal below  $300^\circ\text{C}$ , it means that some H, while retained in the sample, is converted into a form, possibly  $\text{H}_2$ , in which it is not easily detected by RSS. Around the blistering temperature (above  $400^\circ\text{C}$ ), some but not all  $\text{H}_2$  is released, simultaneously with the disappearance of Si-bound H. Finally, around  $625^\circ\text{C}$ , the  $\text{H}_2$  contained in the blisters is desorbed out. For  $6 \times 10^{16} \text{ H/cm}^2$  (Fig. 8b), one can note a first burst at a quite low temperature of  $\sim 330^\circ\text{C}$ , after which a continuous release of  $\text{H}_2$  takes place, together with the decrease of the Raman integrated signal. The final release around  $600^\circ\text{C}$  is prolonged to higher temperature than for  $2 \times 10^{16} \text{ H/cm}^2$ , consistently with the slower decrease of the Raman signal for the higher dose. Blister absence is thus in no way due to unavailability of hydrogen.

The next point is to identify specific structures that may play the critical roles for the fluence dependence of blistering. Figure 9 displays a comparison between a series of spectra taken at successively higher temperatures for both typical fluences. In this figure, it is important to note the different ordinates for the two sets of measurements, illustrating the fact that the Si-bound hydrogen is globally more stable at the higher fluence. In particular, the LFBB is stabler, up to  $300^\circ\text{C}$ , than for the lower dose. Similarly, the peak due to hydrided internal (100) surfaces remains remarkably strong at all temperatures for  $6 \times 10^{16} \text{ H/cm}^2$ . Moreover, as the temperature increases, it becomes sharper while the other ‘background’ diminishes. This indicates the formation of more and more

H-decorated internal surfaces. These structures are generally believed to be the precursors of the larger gas-filled cavities and blisters. And yet, the abundance of these at  $6 \times 10^{16} \text{ H/cm}^2$  does not produce cleaving. In contrast, at  $2 \times 10^{16} \text{ H/cm}^2$ , one notes a conversion of  $\text{VH}_4$  into  $\text{VH}_3/\text{V}_2\text{H}_6$  and a neat dominance of that last structure at  $400\text{--}500^\circ\text{C}$ , i.e. in the blistering temperature range. After blistering, the Si-bound H is quickly lost for  $2 \times 10^{16} \text{ H/cm}^2$ , whereas it is stable in unblistered Si at  $6 \times 10^{16} \text{ H/cm}^2$ . Referring again to the TDS, we believe that the  $\text{H}_2$  released below  $500^\circ\text{C}$  at the lower fluence (Fig. 8a) actually originates from the structures that are observed to disappear progressively in this temperature range, while the  $\text{H}_2$  that fills the blisters comes from the internal desorption of the Si(100):H structures above  $500^\circ\text{C}$ . Finally, the blisters empty out around  $625^\circ\text{C}$ . For  $6 \times 10^{16} \text{ H/cm}^2$  (Fig. 8b), it seems logical to associate the burst at  $\sim 330^\circ\text{C}$  with the collapse of the LFBB above  $300^\circ\text{C}$ , and the retention of H up to high temperature, even above  $700^\circ$ , to the stability of  $\text{VH}_3/\text{V}_2\text{H}_6$  and Si(100):H modes at least up to  $550^\circ\text{C}$ .

## 5 Discussion and conclusion

A number of hypotheses can be made to explain the fluence dependence of blistering. First, we know from our own experience and others’ that amorphous silicon does not blister and one could conjecture that a high H implantation fluence caused amorphisation. However, this hypothesis is negated by the results of Figs. 4 and 5, showing that the random level is not attained even for  $6 \times 10^{16} \text{ H/cm}^2$ . Another hypothesis [25] could be that the H dose actually retained after implantation was much smaller than the incident one. However, both thermal desorption spectrometry and elastic recoil detection analysis (results not shown for brevity) indicate total retention within a few %. An analogy can also be made with a long-known phenomenon, the disappearance of RT helium blistering on metals at extreme fluences ( $\sim 10^{19} \text{ He/cm}^2$ ) [27], then explained by the sputtering away of blister domes and exfoliations produced earlier during the irradiation. For the present fluences, however, sputtering is negligible.

It appears that the presence of the  $\text{VH}_3$  and/or  $\text{V}_2\text{H}_6$  complexes is critical for the initiation of cleaving. The importance of  $\text{VH}_3/\text{V}_2\text{H}_6$  was indeed emphasised in a model by Reborredo et al. [21] based on first-principles calculations of the energies of different configurations. Our findings are then at least compatible with that model. However, the model gives no indication as to why the evolution would proceed differently as a function of the H implantation dose. If the evolution is not determined by the chemical potential, it must be biased by one or several external factors, i.e. other forces than the pure chemical ones. For instance, different types of defects cause mechanical stresses (and therefore strains, e.g. swelling) in the implanted region, and the system will evolve to reduce the local stress. Höchbauer et al. [26] measured the in-plane stress due to 40-keV H implantation in Si and found a compressive stress of  $\sim 250 \text{ MPa}$  at their typical blistering dose of  $5 \times 10^{16} \text{ H/cm}^2$ . They argued that this stress facilitates the separation between the (100) planes in H platelets in (100) silicon and thus favours their enlargement and evolution into flat internal cavities. Interestingly, they also found

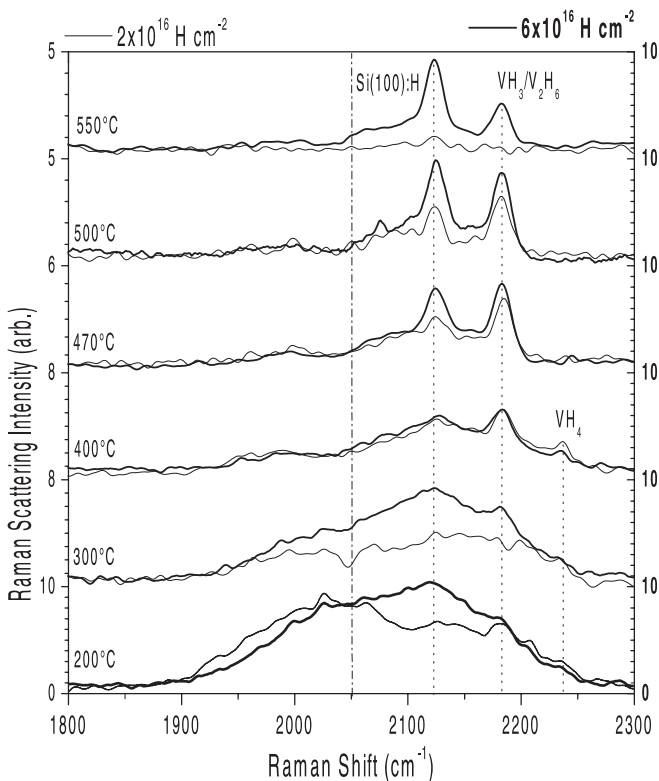


**FIGURE 9** Comparative temperature evolutions of Raman spectra for a blistering fluence ( $2 \times 10^{16} \text{ H/cm}^2$ , thin line, left-hand scale) and a non-blistering fluence ( $6 \times 10^{16} \text{ H/cm}^2$ , thick line, right-hand scale)

that, at somewhat higher fluence ( $\sim 10^{17}$  H/cm<sup>2</sup>), this stress decreased and disappeared; this fact may be relevant for high-fluence blister absence since it would remove one of the factors favouring cleavage.

The peak H concentration is  $\sim 5\%$  [13] at the fluence when blisters first appear and, if we consider the damage profiles (Fig. 5), we can see that the peak interstitial concentration is of the order of 8.5% at that point. Once the thermal evolution has led to internal H-filled cavities, it is near the depth of this peak that cleaving occurs due to the cavities' internal pressure (perhaps aided by the in-plane stress as mentioned above). This is illustrated by the left-hand side of the 'cartoon' shown in Fig. 10. But, for a fluence of  $6 \times 10^{16}$  H/cm<sup>2</sup>, the critical H ( $\sim 5\%$ ) and interstitial ( $\sim 8.5\%$ ) concentrations are reached over a very wide region extending from  $\sim 20$  nm to  $\sim 100$  nm (Fig. 5). The right-hand side of Fig. 10 then illustrates the fact that the pressure in cavities located at one given depth will tend to close up those present at another depth. This will inhibit the in-plane propagation of cracks and the lateral coalescence of cavities, leading to cleaving. Although a net normal force will still exist, giving swelling of the whole implanted area as observed, there will be no clear weak plane at a definite depth at which the crystal may cleave. However, numerous H-filled cavities, which will remain relatively small, will be present, as manifested by the strong Si(100):H signal for the higher H dose at 470–550 °C (Fig. 9). Here, an analogy does apply to RT He blister disappearance, which is actually due to the formation of a wide layer extending to the surface, that is heavily implanted and damaged [28] and nanoporous [29]. Indeed, our TDS measurements show, for all fluences  $\geq 4 \times 10^{16}$  H/cm<sup>2</sup>, a short burst of H<sub>2</sub> at  $< 400$  °C followed by a continuous release (Fig. 8b), suggestive of gas escape through a porous layer, and which is not observed at lower fluence when abundant blistering occurs.

A final effect may be due to fracture toughening at high fluence. Swadener and Nastasi [30] measured the fracture toughness of irradiated Si; however, the irradiation was conducted with Ne ions of  $\geq 100$  keV at RT. Nevertheless, if we scale their results using the displacements per atom (dpa) as a measure of damage, we predict an increase of the fracture toughness of tens of % for  $6 \times 10^{16}$  H/cm<sup>2</sup>. This esti-

mate neglects two effects: the first is that of the Si-H chemistry on the configuration of the defects in H-irradiated Si. This tends to stabilise the defects, in other words to reduce the thermal annihilation of the primary defects. It may then cause stronger fracture toughening than inert-ion irradiation. The other factor neglected is that of the high temperature during the anneal, which is likely to somewhat reduce the toughness.

In summary, silicon cleavage by low-energy H implantation and high-temperature annealing is only possible in a surprisingly narrow window of ion fluence. The study of the defect profiles and the thermal evolution of Si–H stretch modes leads to several conclusions. The triply passivated vacancy complex VH<sub>3</sub> or V<sub>2</sub>H<sub>6</sub> (or both) is the precursor to the formation of large H-containing cavities which, if they grow by crack propagation and coalescence, lead to cleavage. (It would seem that there must be a short-lived or unobservable intermediary in this process, as conjectured earlier [5].) The inhibition of blistering at high fluence is probably mainly due to the widening of the H and defect profiles, which reach, for instance, within 20 nm of the surface for  $6 \times 10^{16}$  H/cm<sup>2</sup>. The resulting stress configuration prevents cleavage at a well-defined depth. The strength and the high-temperature stability of the signal due to H-terminated (100) internal surfaces is the signature of this situation of high-temperature, high-fluence H retention without blistering. At much higher fluence, however, Si finally blisters at room temperature.

**ACKNOWLEDGEMENTS** The authors thank L. Andrzejewski for frequent technical help. This work was supported by funding from the National Science and Engineering Council of Canada and the Fonds Québécois de Recherche sur la Nature et les Technologies at both INRS and UdeM.

## REFERENCES

- 1 S.K. Das, M. Kaminsky: *Adv. Chem. Ser.* **158**, 112 (1976)
- 2 E. Ligeon, A. Guivarc'h: *Radiat. Eff.* **27**, 129 (1976)
- 3 W.K. Chu, R.H. Kastl, R.F. Lever, S. Mader, J. Masters: in *Ion Implantation in Semiconductors*, ed. by F. Chernov, J.A. Borders, D.K. Brice (Plenum, New York 1976) p. 483
- 4 M.K. Weldon, V.E. Marsico, Y.J. Chabal, A. Agarwal, D.J. Eagleham, J. Sapjeta, W.L. Brown, D.C. Jacobson, Y. Caudano, S.B. Christman, E.E. Chaban: *J. Vac. Sci. Technol. B* **15**, 1065 (1997)
- 5 J.K.G. Panitz, D.J. Sharp, C.R. Hills: *J. Vac. Sci. Technol. A* **3**, 1 (1985)
- 6 M. Bruel: *Electron. Lett.* **31**, 1201 (1995)
- 7 M. Bruel: *Nucl. Instrum. Methods B* **108**, 313 (1996)
- 8 Q.Y. Tong, T.H. Lee, K. Gutjahr, S. Hopfe, U. Gösele: *Appl. Phys. Lett.* **70**, 1390 (1997)
- 9 T. Höchbauer, A. Misra, M. Nastasi, J.W. Mayer: *J. Appl. Phys.* **89**, 5980 (2001)
- 10 S.W. Bedell, W.A. Lanford: *J. Appl. Phys.* **90**, 1138 (2001)
- 11 For a review, see G.K. Celler, S. Cristoloveanu: *J. Appl. Phys.* **93**, 4955 (2003)
- 12 B. Terreault: *Surf. Coat. Technol.* **156**, 13 (2002)
- 13 As computed by the binary collision code SRIM; see J.F. Ziegler, J.P. Biersack: [www.srim.org](http://www.srim.org)
- 14 E. Bøgh: *Can. J. Phys.* **46**, 653 (1968)
- 15 J.N. Heyman, J.W. Ager III, E.E. Haller, N.M. Johnson, J. Walker, C.M. Doland: *Phys. Rev. B* **45**, 13 363 (1992)
- 16 Y.J. Chabal, M.K. Weldon, Y. Caudano, B.B. Stefanov, K. Raghavachari: *Physica B* **273**, 152 (1999)
- 17 M. Budde, G. Lüpkke, E. Chen, X. Zhang, N.H. Tolk, L.C. Feldman, E. Tarhan, A.K. Ramdas, M. Stavola: *Phys. Rev. Lett.* **87**, 145 501 (2001)
- 18 E.V. Lavrov, J. Weber, L. Huang, B. Bech Nielsen: *Phys. Rev. B* **64**, 035 204 (2001)
- 19 N. Fukata, T. Otori, M. Suezawa, H. Takahashi: *J. Appl. Phys.* **91**, 5831 (2002)

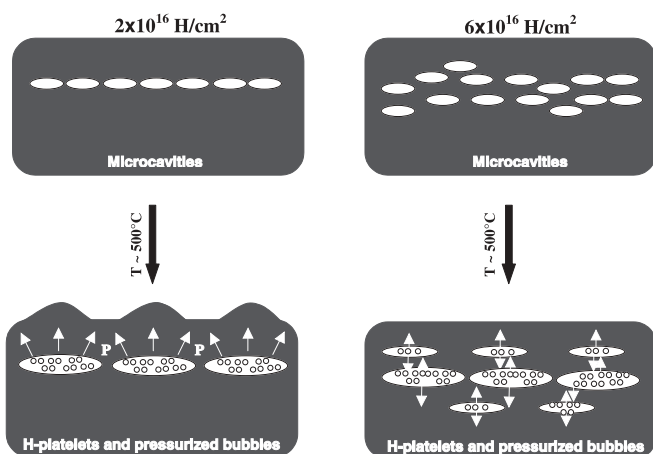


**FIGURE 10** Schematic representations of sub-surface structures for blistering and non-blistering situations

- 20 T. Matsumoto, A.I. Belogorokhov, L.I. Belogorokhova, Y. Masumoto, E.A. Zhukov: *Nanotechnology* **11**, 340 (2000)
- 21 F.A. Reboledo, M. Ferconi, S.T. Pantelides: *Phys. Rev. Lett.* **82**, 4870 (1999)
- 22 O. Moutanabbir, B. Terreault: *J. Chem. Phys.* **121**, 7973 (2004)
- 23 Nanotec Electronica, C/Padilla 1, 28006 Madrid, Spain  
[<http://www.nanotec.es>]
- 24 O. Moutanabbir, A. Giguère, B. Terreault: *Appl. Phys. Lett.* **84**, 3286 (2004)
- 25 X. Lu, N.W. Cheung, M.D. Strathman, P.K. Chu, B. Doyle: *Appl. Phys. Lett.* **71**, 1804 (1997)
- 26 T. Höchbauer, A. Misra, M. Nastasi, J.W. Mayer: *J. Appl. Phys.* **92**, 2335 (2002)
- 27 J.G. Martel, R. St-Jacques, B. Terreault, G. Veilleux: *J. Nucl. Mater.* **53**, 142 (1974)
- 28 B. Terreault: *J. Nucl. Mater.* **93–94**, 707 (1980)
- 29 W. Jäger, J. Roth: *J. Nucl. Mater.* **93–94**, 756 (1980)
- 30 J.G. Swadener, M. Nastasi: *Nucl. Instrum. Methods B* **206**, 937 (2003)